UCLA
UCLA Previously Published Works

Title

Formation and Maintenance of the GEOTRACES Subsurface-Dissolved Iron Maxima in an Ocean Biogeochemistry Model

Permalink

https://escholarship.org/uc/item/10t7p66w

Journal

Global Biogeochemical Cycles, 32(6)

ISSN

0886-6236

Authors

Pham, Anh LD

Ito, Takamitsu

Publication Date

2018-06-01

DOI

10.1029/2017gb005852

Copyright Information

Peer reviewed

![AGU100 ADVANCING EARTH AND SPACE SCIENCE]

Global Biogeochemical Cycles

Key Points:
- An ocean biogeochemistry model is used to better understand the extrema of subsurface-dissolved iron observed in the GEOTRACES transects
- The iron maxima are formed by release of scavenged iron in high-dust regions and by sedimentary or hydrothermal inputs in low-dust regions
- Dissolved iron is sensitive to the pattern and binding strength of the subsurface ligand

Supporting Information:
- Supporting Information S1
- Table S1
- Figure S1

Correspondence to:
A. L. D. Pham,
anh.pham@eas.gatech.edu

Formation and Maintenance of the GEOTRACES Subsurface-Dissolved Iron Maxima in an Ocean Biogeochemistry Model

Anh L. D. Pham[1] [ID] and **Takamitsu Ito**[1] [ID]

[1]School of Earth and Atmospheric Sciences, Georgia Institute of Technology, Atlanta, GA, USA

Abstract Recent GEOTRACES transects revealed basin-scale patterns of dissolved iron in the global oceans, providing a unique opportunity to test numerical models and to improve our understanding of the iron cycling. Subsurface maxima of dissolved iron in the upper ocean thermocline are observed in various transects, which can play an important role in regulating marine productivity due to their proximity to the surface euphotic layer. An ocean biogeochemistry model with refined parameterizations of iron cycling is used to examine the mechanisms controlling the formation and maintenance of these subsurface maxima. The model includes the representation of three iron sources including dust deposition, continental shelves, and hydrothermal vents. Two classes of organic ligands are parameterized based on the dissolved organic matter and apparent oxygen utilization. Parameterizations of particle-dependent scavenging and desorption are included. Although the model still struggles in fully capturing the observed dissolved iron distribution, it starts reproducing some major features, especially in the main thermocline. A suite of numerical sensitivity experiments suggests that the release of scavenged iron associated with sinking organic particles forms the subsurface-dissolved iron maxima in high-dust regions of the Indian and Atlantic Oceans. In low-dust regions of the Pacific basin, the subsurface-dissolved iron extrema are sustained by inputs from the continental shelves or hydrothermal vents. In all cases, subsurface ligands produced by the remineralization of organic particles retain the dissolved iron and play a central role in the maintenance of the subsurface maxima in our model. Thus, the parameterization of subsurface ligands has a far-reaching impact on the representation of global iron cycling and biological productivity in ocean biogeochemistry models.

1. Introduction

The micronutrient iron (Fe) limits the biological productivity of about half of the world's oceans including the subpolar Pacific, the equatorial Pacific, and the Southern Ocean, thereby influencing the marine ecosystems and global carbon cycle (Boyd & Ellwood, 2010; Moore et al., 2013). For this reason, processes driving the ocean Fe cycling have been studied intensely over past decades. Oceanic Fe cycling is distinct from those of other nutrients because of the extremely low concentration of dissolved Fe (dFe) and the involvement of diverse and complex array of processes. In the oxygenated seawater, Fe mostly exists as ferric (Fe(III)) species with the solubility at a subnanomolar level (Liu & Millero, 2002) and thus rapidly precipitates to form colloidal Fe oxides (Wu et al., 2001). The very low concentration of dFe has made it difficult to accurately determine its global distribution. At the same time, the diverse source and sink processes and their interactions pose a significant modeling challenge. Ocean biogeochemistry models integrate these mechanisms and their interactions in the context of the global ocean circulation and have indeed provided important insights, but the models still show significant biases (Tagliabue et al., 2016, 2017). The existence of significant model biases indicates problems in the current parameterizations of Fe cycling and the quantification of Fe sources and sinks.

There are several sources of Fe to the ocean including atmospheric deposition (Duce & Tindale, 1991; Jickells et al., 2005), continental shelves (Elrod et al., 2004; Johnson et al., 1999), and hydrothermal vents (Fitzsimmons et al., 2014; Resing et al., 2015; Tagliabue et al., 2010). There are also multiple processes removing Fe from the seawater such as biological uptake (Sunda, 2012), precipitation, and scavenging onto organic and inorganic particles (Dutay et al., 2015; Jackson & Burd, 2015). Furthermore, Fe can take many different forms in the water column. As stated earlier, ferric (Fe(III)) species, the primary form of Fe in the seawater, has the solubility

at a subnanomolar level and thus quickly precipitates. Fe can also be bound to marine particles either through the biological incorporation or scavenging process (Revels et al., 2015). The particle-bound Fe, referred to as particulate Fe, can aggregate and gravitationally sink through the water column (Fowler & Knauer, 1986; Jeandel et al., 2015). Some of the sinking particulate Fe can return to dissolved form through desorption and particle remineralization (Boyd et al., 2000). Remineralized Fe can be scavenged again or be transported back to the surface via upwelling and vertical mixing (Tagliabue, Sallee, et al., 2014). However, dFe can be protected from scavenging and precipitation by forming complexes with organic ligands (Macrellis et al., 2001; van den Berg, 1995). The crucial role of organic ligands in protecting dFe was first demonstrated by Rue and Bruland (1995), who showed that the majority of dFe in seawater (~99%) is bound to ligands. Recent observational and experimental studies further confirmed the vital role of ligands by showing that marine bacteria produces ligands to facilitate the retention and biological uptake of dFe (Buck et al., 2010; Kustka et al., 2015; Rue & Bruland, 1995).

There is an emerging opportunity to improve our understanding of these processes as quality-controlled Fe data set is rapidly expanding along the GEOTRACES transects (Mawji et al., 2015). These transects confirmed the existence of subsurface dFe extrema as a prominent feature in many parts of the oceans, which was first discovered by Johnson et al. (1997) through various vertical Fe profiles in the Pacific, North Atlantic, and Southern Oceans. A common pattern of dFe maxima has been observed by GEOTRACES cruises in the main thermocline (300-1,000 m) as well as in the deep waters (>2,000 m) of various ocean basins. The thermocline dFe maxima are likely formed by the release of Fe from remineralization processes (Nishioka et al., 2013; Noble et al., 2012; Rijkenberg et al., 2014) and/or by the external Fe sources (Nishioka & Obata, 2017; Resing et al., 2015). The deep (>2,000 m) dFe maxima are likely associated with hydrothermal sources (Nishioka et al., 2013; Resing et al., 2015). This study will focus on the middepth dFe maxima embedded in the main thermocline due to their proximity to the surface euphotic layer with a potential to influence biological productivity. The upwelling of thermocline waters can be an important source of dFe to the marine phytoplankton, especially for the Fe-limited upwelling regions (Tagliabue, Sallee, et al., 2014).

The objective of this study is twofold. First, we aim to test the ability of an ocean biogeochemistry model to reproduce the subsurface dFe maxima observed in the new GEOTRACES transects. The model includes a number of refinements in the Fe cycle parameterizations including two classes of spatially varying organic ligands, scavenging onto and desorption from organic and inorganic particles, and inputs from external sources. Second, we aim to better understand the mechanisms supporting the formation and maintenance of the subsurface dFe maxima through a suite of sensitivity experiments. We purposefully turn off the Fe cycling parameterizations one at a time. The importance of a specific mechanism is inferred from the disruption in the dFe distribution caused by its removal from the model, indicating its contribution to the model's ability to reproduce the observed dFe distribution.

We specifically examine parameterizations controlling the transformation of Fe between dissolved and particulate pool via scavenging, desorption, and remineralization mediated by the presence of organic ligands. Organic ligands bind with dFe and prevent it from being scavenged onto marine particles, thus playing central roles in the retention of Fe in the dissolved pool (Hutchins & Boyd, 2016). The sources, sinks, and molecular identities of organic ligands are not yet fully understood (Hassler et al., 2017), and the parameterizations of organic ligands in ocean biogeochemistry models still have significant uncertainty. While there can be many different types of ligands in the oceans (Hunter & Boyd, 2007), existing measurements often simply define two discrete ligand classes based on their distribution and binding strength with dFe measured by the conditional stability constant K_n: a stronger, surface ligand (L_1) and a weaker, subsurface ligand (L_2). Several approaches have been taken to represent ligands in ocean biogeochemistry models. Earlier generations of models assumed a spatially homogeneous single ligand by either limiting the scavenging at a constant threshold (Archer & Johnson, 2000) or explicitly resolving the local partitioning of free and ligand-bound Fe (Parekh et al., 2005). Subsequent development included the spatially variable ligand distribution, often by linking it to the pattern of dissolved organic matter and/or apparent oxygen utilization (AOU; Misumi et al., 2013; Tagliabue & Völker, 2011). The uncertainties in the representation of ligands can lead to biases in the model dFe distribution (Tagliabue et al., 2016). However, observational techniques to identify Fe-ligand complex are being improved (Boiteau & Repeta, 2015) and the data coverage for organic ligands is expanding in recent years (Buck et al., 2015; Gerringa et al., 2015), providing an opportunity to improve ligand parameterizations. A recent modeling study by Völker and Tagliabue (2015) explicitly simulated a single ligand as a prognostic variable by representing its sources and sinks. While it requires specifications of the ligand sources and sinks

that are still uncertain, the inclusion of a prognostic ligand clearly improved the subsurface dFe distribution in ocean biogeochemistry models (Tagliabue et al., 2016). This study takes a relatively simple approach where ligands are parameterized based on calibrating empirical coefficients against the available observations. The parameterization itself is not new; we aim to keep the algorithm as simple as possible while still capturing the essential mechanisms as demonstrated by earlier studies (Misumi et al., 2013; Tagliabue & Völker, 2011). This approach is simple to implement and delivers spatially resolved representation of organic ligands and thus can be easily manipulated in the sensitivity experiments.

The paper is organized as follows. In section 2, we describe the model configuration and set up the experimental design. In sections 3 and 4, we present results of sensitivity experiments. In section 5, we summarize and discuss the implication of these results.

2. Model Configuration and Experimental Design

The ocean biogeochemistry model used in this study is based on the Massachusetts Institute of Technology general circulation model (Marshall, Adcroft et al., 1997; Marshall, Hill et al., 1997), configured for a global bathymetry in a $1° \times 1°$ longitude-latitude grid and 23 nonuniform vertical z levels. At this resolution, mesoscale eddies are parameterized using the isopycnal tracer and thickness diffusion scheme (Gent & Mcwilliams, 1990; Redi, 1982; Solomon, 1971) and the mixed-layer processes are parameterized using the K-Profile Parameterization scheme (Large et al., 1994). The model is run offline, using the climatological monthly circulation fields taken from the Estimating the Circulation and Climate of the Ocean product version 3 (Wunsch & Heimbach, 2007). The biogeochemical component of the model is modified from Parekh et al. (2005, hereafter P05) and Dutkiewicz et al. (2005, hereafter D05), which carries dissolved inorganic carbon, alkalinity, phosphate (PO_4^{3-}), dissolved organic phosphorus (DOP), dFe, and oxygen (O_2). Biological productivity is controlled by the availability of light and nutrients (PO_4^{3-} and dFe) using Monod function. There are some notable differences in the parameterization of the Fe cycling relative to the earlier version of Massachusetts Institute of Technology general circulation model in P05 and D05. In this study, the biological Fe uptake in the subarctic Pacific and Southern Oceans can be varied as a function of the dFe concentration, which represents the luxury Fe uptake of diatoms in these regions where silica is abundant (Ingall et al., 2013). In addition, we include three external sources of dFe (atmospheric deposition, continental shelves, and hydrothermal vents) as opposed to only atmospheric deposition as in P05 and D05.

2.1. Atmospheric Dust Deposition
Atmospheric deposition of dFe under the preindustrial condition is obtained from recent modeling studies, which employed the three-dimensional atmospheric chemical transport model GEOS-Chem coupled with a comprehensive dust-Fe dissolution scheme (Ito et al., 2016; Johnson & Meskhidze, 2013). The solubility of dust Fe is spatially varying. The majority of the deposited dust Fe is likely in the insoluble form especially in the high-dust region. Ocean biogeochemistry models tend to overestimate the surface dFe concentration under high-dust regions in the Indian and tropical Atlantic Oceans if a uniform solubility is used (Tagliabue et al., 2016). Thus, we manipulate the solubility of dust Fe for these regions, reducing it by 2 orders of magnitude. We acknowledge the limitation of this approach and are aware of a new approach from Ye and Völker (2017) by explicitly solving for lithogenic particles; however, there is still large uncertainty in the dissolution kinetics of particulate dust Fe (Mahowald et al., 2009) and in the magnitude of dust deposition itself (Anderson et al., 2016).

2.2. Shelf Sediments
The input of dFe from seafloor sediments is calculated by following Moore and Braucher (2008). The essence of this parameterization is to represent the release of Fe from unresolved continental shelves in the coarse-resolution ocean model. To do so, we first estimate the biological productivity over the continental shelves using remotely sensed ocean color data (Behrenfeld & Falkowski, 1997). Second, we calculate the e-ratio as a function of total productivity and sea surface temperature, following Laws et al. (2011), and assume a parameterized remineralization profile below the euphotic layer (Martin et al., 1987) to estimate the sinking organic flux at the depths of continental shelves using the ETOPO2 (2-min global ocean bathymetry). The sedimentary dFe flux is then calculated and mapped onto the coarse-resolution model grid points based on a ratio with the organic carbon flux (Elrod et al., 2004). Using the World Ocean Atlas oxygen data (Garcia & Gordon, 1992), this ratio is set to 0.68×10^{-3}, which is the same as in Elrod et al. (2004), for the low-oxygen waters ($[O_2] < 30$ μM) but is reduced by 1 order of magnitude for well-oxygenated regions ($[O_2] > 30$ μM).

2.3. Hydrothermal Vents

The hydrothermal dFe flux is scaled with ^{3}He flux, following Tagliabue et al. (2010) with some modifications. Previous work reported the mismatches of hydrothermal dFe signals between state-of-the-art Fe biogeochemistry models and observations (Tagliabue et al., 2016; Tagliabue & Resing, 2016), especially along the slow-spreading ridges (Saito et al., 2013). The coefficient relating the hydrothermal dFe to ^{3}He fluxes is unlikely a uniform constant; thus, we vary it for different ocean basins. The same ratio as in Tagliabue et al. (2010) is used for the Southern Ocean but is increased by a factor of 80 in the Atlantic Ocean as suggested by Saito et al. (2013) and by a factor of 10 and 10^3 for the Indian and Pacific Oceans, respectively, to better match observations (Nishioka et al., 2013; Resing et al., 2015).

2.4. Organic Ligands

Following previous studies by Tagliabue and Völker (2011, hereafter TV11) and Misumi et al. (2013, hereafter M13), we parameterize two ligand classes as functions of dissolved organic carbon (DOC) and AOU. The two ligand classes (L_1 and L_2) have different binding strengths to the total free dFe in the seawater. This is an improvement from the previous studies of P05 and D05 which uses a single, uniform organic ligand. Of the two ligands, L_1 is considered to have a stronger binding strength ($K_{L1} = 10^{12}$ L/mol) and L_2 has a weaker binding strength ($K_{L2} = 10^{11}$ L/mol). Based on previous studies, we assume that L_1 is primarily composed of the biologically produced siderophores with relatively high conditional stability constant (Adly et al., 2015; Macrellis et al., 2001). L_2 is assumed to be primarily composed of humics, which may be produced by the remineralization of the particulate organic matter (Laglera & van den Berg, 2009; Velasquez et al., 2016; Vraspir & Butler, 2009). However, the binding strength for humic-like ligand is not certain, as some studies suggested it to be weaker than 10^{11} L/mol (Gledhill & Buck, 2012). Based on these assumptions, we parameterize the spatial distributions of L_1 and L_2 as linear functions of DOC and AOU as shown in equations (1) and (2).

$$L_1 = \alpha[\text{DOC}_\text{labile}] \tag{1}$$

$$L_2 = \gamma\beta[\text{AOU}] + (1 - \gamma)[L_{2\text{refract}}] \tag{2}$$

α is calibrated based on the observed surface ligand and labile DOC distributions along the GA02 western Atlantic transect, where we assume the observed minimum DOC as the proxy for the labile component of DOC (Gerringa et al., 2015; Middag et al., 2015; Salt et al., 2015). The empirical coefficients for L_2 (β and γ) are calibrated by fitting to the observed ligand distribution along the GEOTRACES transects (Mawji et al., 2015) in a least squares sense. In the model, DOC_labile is represented in terms of DOP and is calculated as $\text{DOC}_\text{labile} = R_{\text{CP}}\text{DOP}$, where R_{CP} (set to 120) is the stoichiometric C:P ratio of the organic matter. DOP in the model is generated by photosynthesis and has an e-folding decay timescale of 6 months. The mean magnitude of DOC_labile in our model is generally an order of magnitude smaller than the mean magnitude of observed minimum DOC along the GA02 transect ($\mathcal{O}(0.1~\mu\text{M})$ versus $\mathcal{O}(1~\mu\text{M})$); thus, we increase the magnitude of α by a factor of 10 in order to reproduce the observed magnitude of L_1. β is calibrated based on the observed subsurface ligand and AOU along two oceanic transects (the GA02 and GA03 — subtropical North Atlantic Ocean; Buck et al., 2015; Middag et al., 2015; Voelker et al., 2015). AOU is calculated from dissolved O_2, temperature, and salinity data (Garcia & Gordon, 1992). Parameterizing L_2 in terms of AOU leads to an artificial loss of ligand when the subsurface waters upwell to the surface and AOU decreases to zero on the timescale of air-sea O_2 exchange (~1 month). Although the decay of AOU in the surface waters could be analogous to the photochemical loss of ligands reported in a previous study (Barbeau et al., 2001), we acknowledge that it may cause biases in the ligand parameterization. We also include $L_{2\text{refract}}$ as a constant background that represents the highly refractory component of DOC (Hassler et al., 2011). It is important to note that this parameterization is fundamentally limited by the availability of observational data to calibrate the coefficients, and the ligand parameters and formulations may need to be updated as more data become available in the future. With these limitations in mind, two classes of spatially varying organic ligands are used to solve for the dFe complex in the model. The binding of free Fe with the two ligand classes is solved iteratively as described in the supporting information (S1).

2.5. Scavenging

The free Fe (Fe') that is not bound to ligands is subject to scavenging losses by three mechanisms. First, Fe' can be scavenged onto particulate organic matter based on a first-order bulk scavenging rate following

Parekh et al. (2005) and Galbraith et al. (2010). This scavenging process is parameterized as a function of the concentration of the particulate organic matter and the Fe' concentration

$$\text{Fe}_{\text{scav}}^{\text{org}} = K_{\text{org}} C_p^{0.58} [\text{Fe}']$$

(3)

where K_{org} is the rate constant and C_p is the particulate organic matter concentration. In this model, the concentration of particulate organic matter is not a prognostic variable and its vertical attenuation with depth is crudely parameterized as a power function modified from Martin et al. (1987). C_p is diagnosed from the sinking particle flux and its assumed sinking speed. The exponent of 0.58 follows the empirical study of Honeyman et al. (1988).

Fe scavenged through this mechanism can be released back to the water column through the dissolution/remineralization of sinking organic particles (Boyd et al., 2010). The model calculates dFe released from organic particles in two components: cellular Fe and scavenged Fe. Remineralization of cellular Fe is determined by the Martin curve and the Fe:P uptake ratio. Because of scavenging and dissolution processes, the stoichiometric Fe:P ratio (R_{FeP}) of organic particles can change along the sinking pathway. The model explicitly calculates the vertically variable R_{FeP} by integrating the particulate Fe mass balance and determines the vertical profile of Fe release from organic particles. A detailed description of this parameterization is provided in the supporting information (S2).

Second, Fe' can be scavenged onto inorganic particles, which are not produced by biological processes and may have lithogenic origin (Boyd et al., 2010; Galbraith et al., 2010; Tagliabue, Aumont, et al., 2014). As in Galbraith et al. (2010), the inorganic scavenging is parameterized as a first-order loss process with a rate coefficient, K_{inorg},

$$\text{Fe}_{\text{scav}}^{\text{inorg}} = K_{\text{inorg}} [\text{Fe}']$$

(4)

Elevated dust deposition enhances the inorganic scavenging process because of the increase in lithogenic particle concentration under high dust deposition (Ye & Völker, 2017). Therefore, we scale the rate constant by the dFe flux from atmospheric deposition. The scavenged Fe through this mechanism can also return to the water column by desorption from sinking particles. This return dFe flux is calculated in the model from the vertical profile of sinking inorganic scavenged Fe flux, which is represented by a power function with a coefficient of −0.4.

Finally, another scavenging loss process represents the precipitation of Fe' (Fitzsimmons et al., 2015; Honeyman & Santschi, 1989). The solubility of Fe' is very low in the oxygenated seawater (Liu & Millero, 2002); therefore, the model removes the excess concentration of Fe' that is beyond the Fe solubility, [Fe'$_{\text{max}}$], set to 0.3 nM. We acknowledge the crude parameterization of this type of Fe' loss, but it occurs only in a small fraction of the model domain with an intense Fe deposition. In addition, another potential loss mechanism for dFe by the coagulation of colloidal Fe (defined by the filter size usually between 0.02 and 0.2 μm), which is termed colloidal pumping (Honeyman & Santschi, 1989; Tagliabue et al., 2016), is not yet represented in our model. The model Fe cycling is schematically illustrated in supporting information Figure S1.

2.6. Experimental Design

The model was spun up for 1,000 years to achieve a quasi steady state with the standard set of parameters (*Full* run). At the end of the spin-up, the model drifts in the global inventories of dFe (<0.01%/year) and the biological carbon uptake (< 0.02%/year) are minimal. Six sensitivity experiments are initialized from the end of the spin-up run with altered parameterizations and integrated for additional 1,000 years to reach new quasi steady state. The purpose of these simulations is to evaluate the relative roles of organic ligands, scavenging, remineralization processes, and external sources in regulating the ocean dFe cycling. The six experiments are designed as follows.

1. *constL* run uses a uniform constant concentration for ligand (1 nM) with $K_L = 10^{11}$ mol/L.
2. *constK$_L$* run uses the same conditional stability constant for L$_1$ and L$_2$ (set to $10^{11.5}$ mol/L).
3. *Large ΔK_L* run uses increased difference in the conditional stability constants between L$_1$ (set to 10^{13} mol/L) and L$_2$ (set to 10^{10} mol/L).
4. *No Fe redissolution* run suppresses the dissolution of scavenged Fe associated with organic particles.
5. *Weak sed* run reduces the shelf Fe source by 70%.
6. *Weak hydro* run reduces the hydrothermal Fe source by applying a uniform dFe/^{3}He ratio as in Tagliabue et al. (2010).

The first three sensitivity runs will examine different aspects of the ligand parameterization. Comparing *constL* and *Full* run will illustrate the importance of the nonuniform ligand distribution. In contrast, *constK$_L$* and *Large ΔK$_L$* runs will show the importance of different binding strengths between the two types of ligand. The last three runs will examine different sources of Fe to the water column. Scavenging of Fe' onto particulate organic matter is a major removal process of dFe, but the scavenged Fe can return to dissolved form in the deeper waters when particles are remineralized. Thus, sinking organic particles can effectively transfer dFe downward in the water column. In the *No Fe redissolution* run, this process is suppressed in order to assess the importance of the coupled scavenging-dissolution process as a subsurface source of dFe. Other model parameters for *Full* and sensitivity runs are provided in supporting information Table S1.

## 3. Mechanism Behind the Subsurface DFE Maxima

The annual mean of the last year output dFe distribution of the model is compared with observations in six GEOTRACES transects: the GA02 (Figure 2, Rijkenberg et al., 2014), CoFeMUG (Figure 3, Noble et al., 2012; Saito et al., 2013), GI04 (Figure 4, Nishioka et al., 2013), 02 (Figure 5, Nishioka & Obata, 2017), GP13 (Figure 6, Ellwood et al., 2018), and GP16 (Figure 7, Resing et al., 2015). While comparing the annual mean dFe output with GEOTRACES dFe data could lead to some mismatches due to large seasonal changes in surface observations (Sedwick et al., 2005; Wu & Boyle, 2002), these comparisons can still give us insight on how our model performs and improve our understanding of the subsurface dFe distributions. Observational dFe data are obtained from the GEOTRACES 2017 intermediate data products (Mawji et al., 2015), and we used the objective mapping method to interpolate model and observational dFe data onto the same grid which has spatial resolution of 1° and vertical resolution of 10 m near the surface to 100 m at depth. More details on the model-data comparison method are provided in the supporting information (S3). The surface model dFe concentration is low in the subpolar North Pacific, the tropical Pacific, and the Southern Oceans and is high in the tropical Atlantic and Indian Oceans because of their proximity to major dust sources (Figure 1).

The two transects covering the Atlantic basin reveal unique features of the dFe distribution that are distinct from macronutrients. Specifically, dFe shows weak signature of major water masses likely due to the distinct patterns of sources and sinks such as atmospheric deposition, continental shelves, and particle scavenging (Rijkenberg et al., 2014).

The Indian Ocean transect displays a stark contrast in the dFe distribution between the tropical and subtropical waters (Figure 4a, Nishioka et al., 2013). The three Pacific basin transects display typical features of the dFe distribution for high-nutrient low-chlorophyll regions. The low dFe concentration is ubiquitous at the surface despite the high dFe levels in the subsurface and deep waters, which are supplied from the low-oxygen continental shelves and hydrothermal vents (Nishioka & Obata, 2017; Resing et al., 2015). All these transects show a pattern of dFe maximum at around 300- to 1,000-m depth, typically near the oxygen minimum layer and thus can be a signal of remineralization process (Nishioka et al., 2013; Noble et al., 2012; Rijkenberg et al., 2014). We focus on the model-data comparison for the upper 1,000 m by expanding the depth from 0 to 1,000 m and compressing the rest of the water column in Figures 2–7. While the model shows biases in dFe distribution, some general features of the subsurface dFe maxima are reproduced, especially in the main thermocline.

3.1. Atlantic and Indian Oceans

The GA02 section maps the meridional dFe distribution along the western Atlantic basin (Rijkenberg et al., 2014). The surface dFe enrichment around 20°N and the strong dFe maximum around 300–1,000 m at 10°N are both reproduced in the *Full* run of the model (Figures 2a and 2b), but our model displaces the depth of the subsurface dFe peak to a shallower depth than observed (~400 m in the model versus ~600-m depth in the observation). Our model also underestimates the magnitude of the surface dFe at 20°N about 0.4 nM. The model also reproduces the elevated subsurface dFe observed at 35–40°S but underestimates its magnitude and somewhat displaces its location further south than observations. This feature, which is not captured by most models analyzed in Tagliabue et al. (2016), might be explained by the dFe flux from shelves or the Rio de la Plata River (Rijkenberg et al., 2014). Another model bias is in the subsurface waters around 40°N, where our model captures the observed dFe maximum from 400 to 1,000 m, but its extension is up to the surface, while observed surface dFe is low. Several other models mentioned in Tagliabue et al. (2016) also have this problem, and it may indicate bias in the scavenging scheme. Our model also fails to capture features of the hydrothermal signal in the deep ocean. Specifically, the modeled hydrothermal dFe signal seems to be displaced and overestimated, especially around 2,000–3,000 m at 20–30°S. Although the model exhibits some biases,
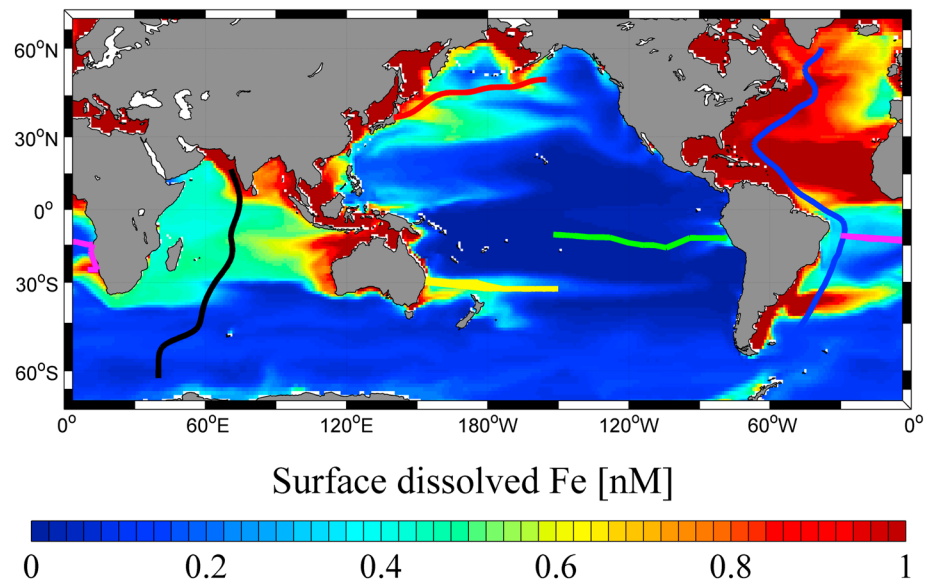
Figure 1. Modeled (*Full* run) surface dFe distribution (black, red, yellow, green, blue, and magenta lines indicate cruise tracks of GI04, GP02, GP13, GP16, GA02, and CoFeMUG cruises from GEOTRACES, respectively). dFe = dissolved Fe.

we find the overall results encouraging. With the inclusion of a relatively simple, spatially varying ligand parameterization, the model starts to reproduce the observed subsurface dFe maxima at 10°N and at 35–40°S, which were not captured by Dutkiewicz et al. (2015) whose Fe cycling is based on the earlier version of our model.

The mechanism behind the observed subsurface maxima is explored through six additional sensitivity experiments. Figures 2–7 shows a subset of the sensitivity runs. The *constL* and *No Fe rediss.* runs, respectively, suppress the release of ligand and scavenged Fe associated with organic particles. The *Weak sed* and *Weak hydro* runs reduce the Fe input from continental shelves and hydrothermal vents, respectively. The subsurface maximum of dFe at 10°N disappears in both *constL* and *No Fe rediss.* runs (Figures 2c and 2d), whereas it almost stays intact in *Weak sed* and *Weak hydro* runs. Similarly, the subsurface-rich dFe water at 40°N is greatly decreased in the *constL* and *No Fe rediss.* runs but just slightly decreases in the other two experiments. On the other hand, the elevated subsurface dFe at 35–40°S is significantly reduced in *constL*, *Weak sed*, and *No Fe rediss.* runs. The *Weak hydro* experiment shows the decrease of dFe only in the deep ocean (Figure 2f) where the hydrothermal dFe flux dominates. These results suggest that the remineralization sources of ligand and dFe are required to sustain the observed dFe subsurface maxima in the GA02 western Atlantic transect. In addition, the shelf Fe source might be important for the subsurface dFe concentration in the South Atlantic.

The CoFeMUG section maps the horizontal dFe distribution along the subtropical South Atlantic (Noble et al., 2012; Saito et al., 2013). The subsurface dFe maximum around 300–800 m at 8–10°E near the eastern margin is captured in the *Full* run, but its magnitude is underestimated while its westward extension is overestimated (Figures 3a and 3b). This maximum is suggested to be associated with remineralization process and/or sediment input from continental shelves (Noble et al., 2012). Our model cannot reproduce the elevated hydrothermal dFe concentration around 3,000 m at 15°W, and it generally underestimates the deep dFe concentration along this transect. The mechanism behind the observed subsurface dFe maximum is explored through four sensitivity experiments (Figures 3c–3f). Similar to the GA02 transect, the subsurface maximum of dFe disappears in both the *constL* (Figure 3c) and *No Fe redis.* (Figure 3d) runs. In the *Weak sed* run, this feature is reduced in magnitude (Figure 3e). In the *Weak hydro* run, only the hydrothermal Fe signal in the western part of the transect at 3,000 m is reduced (Figure 3f). These results suggest that the observed subsurface dFe maximum in the CoFeMUG subtropical South Atlantic transect is formed mostly by the simultaneous release of ligand and dFe from organic particles, with the sedimentary Fe flux acting as an additional contributing factor.
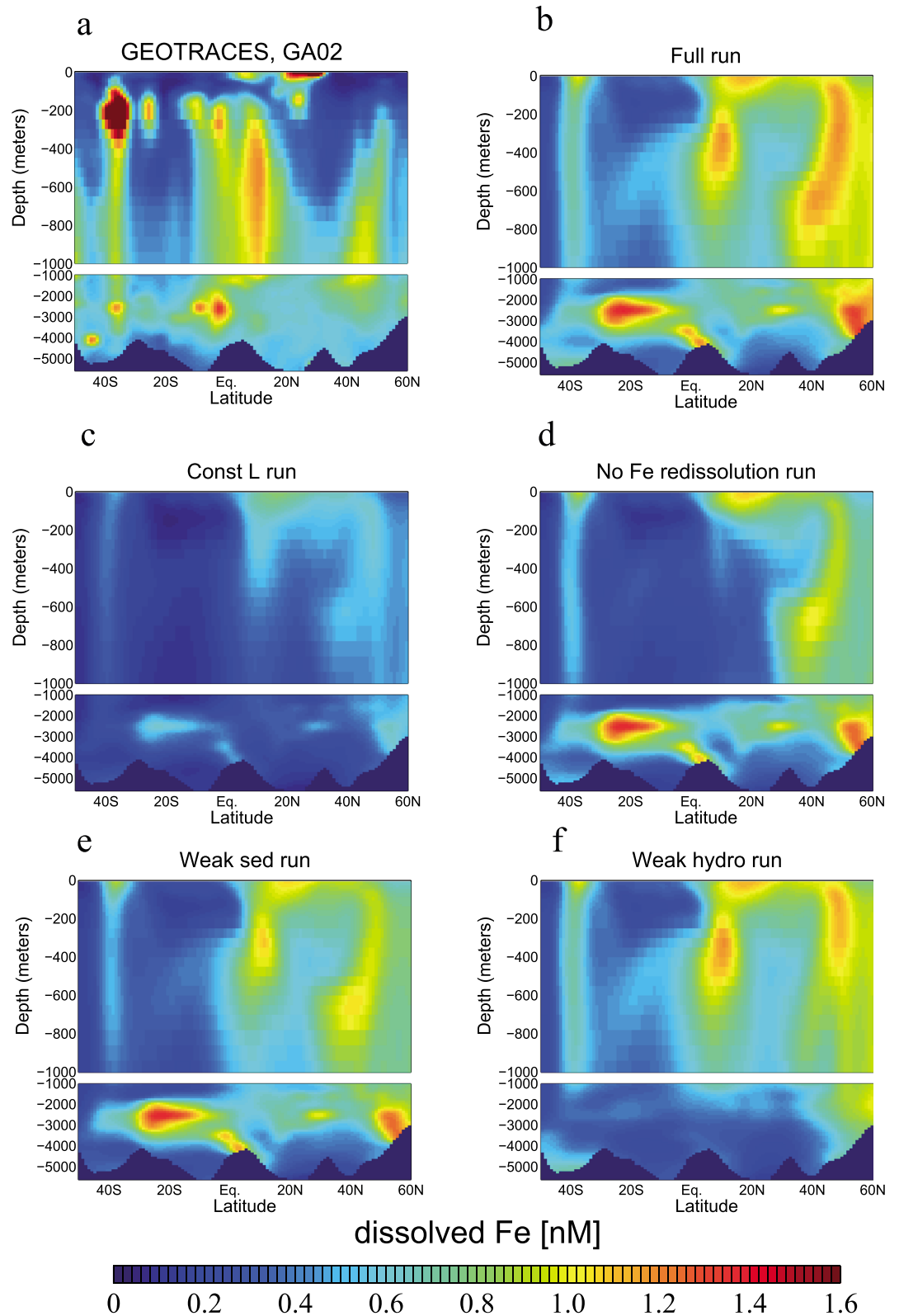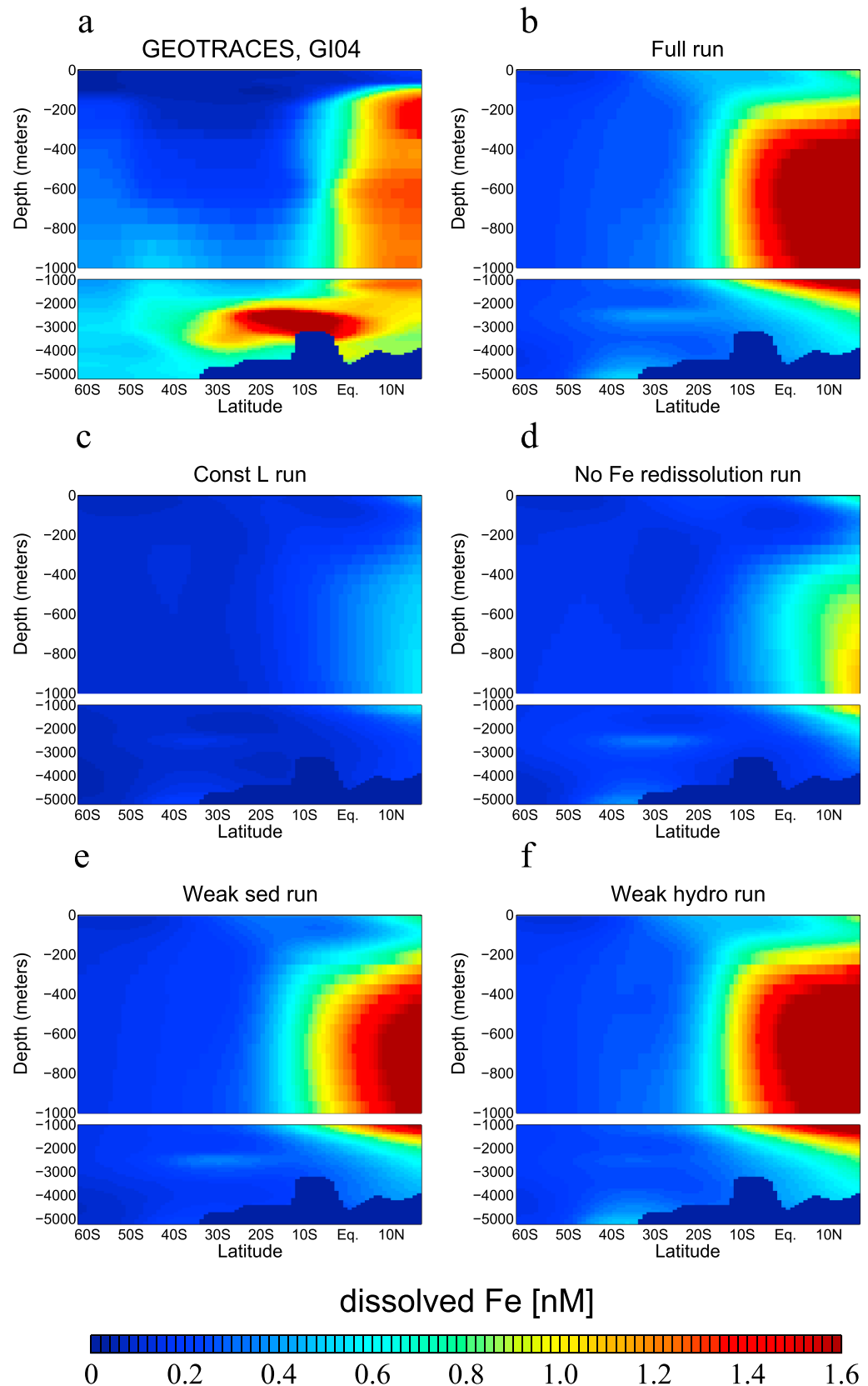
Figure 2. dFe distribution along the GA02 transect: (a) observations, (b) *Full* run, (c) *ConstL* run, (d) *No Fe redissolution* run, (e) *Weak sed* run, and (f) *Weak hydro* run. dFe = dissolved Fe.
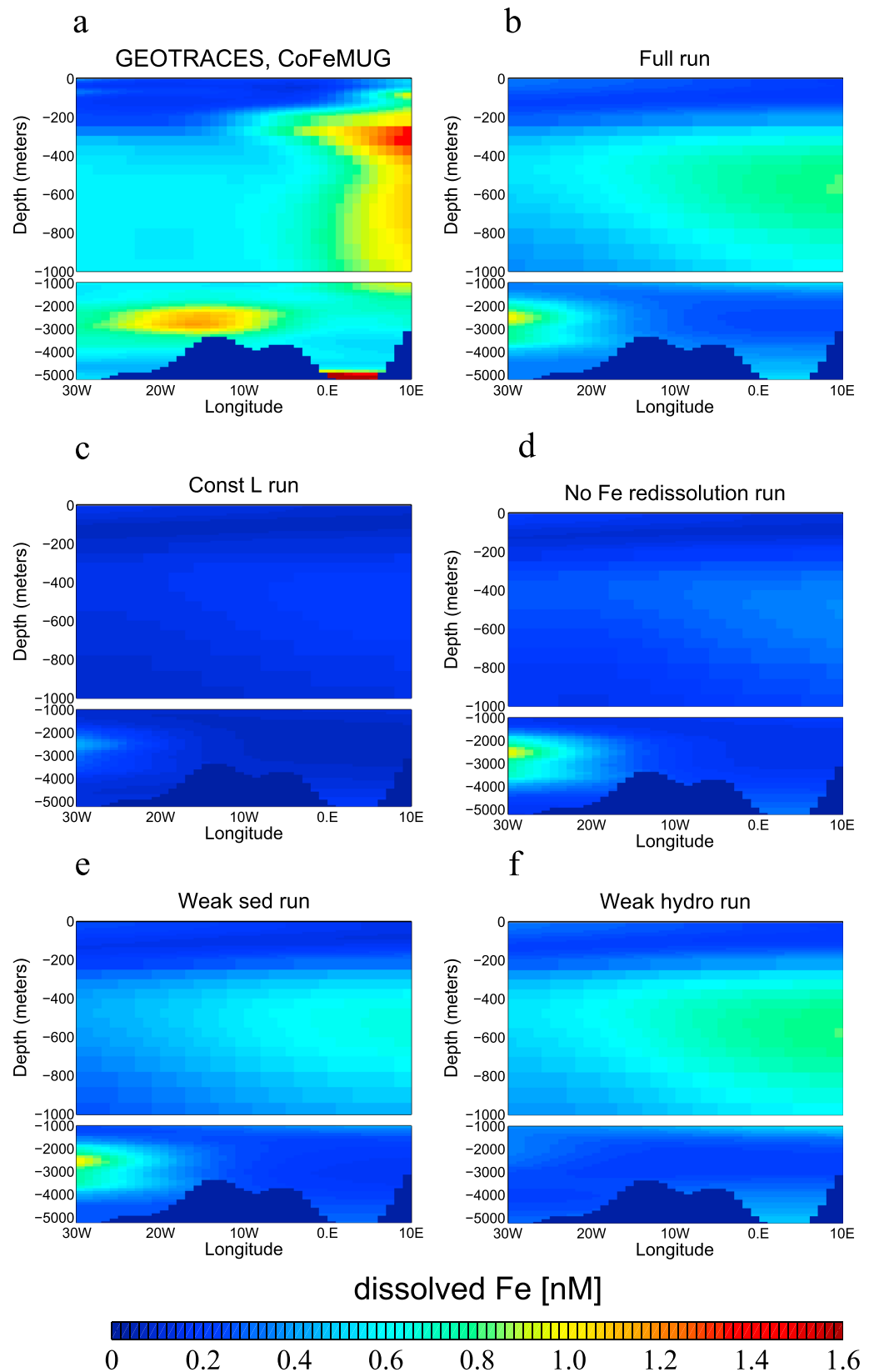
Figure 3. dFe distribution along the CoFeMUG transect: (a) observations, (b) *Full* run, (c) *ConstL* run, (d) *No Fe redissolution* run, (e) *Weak sed* run, and (f) *Weak hydro* run. dFe = dissolved Fe.

Figure 4. dFe distribution along the GI04 transect: (a) observations, (b) *Full* run, (c) *ConstL* run, (d)*No Fe redissolution* run, (e) *Weak sed* run, and (f) *Weak hydro* run. dFe = dissolved Fe.

The GI04 section maps the meridional dFe distribution in the Indian Ocean (Nishioka et al., 2013; Figure 4). The model captures the pattern of upper ocean dFe distribution reasonably well in this region (Figures 4a and 4b). Specifically, the model captures the strong meridional gradient of dFe centered at around 10°S where the tropical thermocline exhibits the highest dFe concentration. The model also reproduces the subsurface peak of dFe in the north Arabian Sea (~10°N), but its amplitude and extension are overestimated. This feature could be formed by remineralization and/or adjacent reducing sediments (Nishioka et al., 2013). The model also overestimates the surface dFe concentration around 10°N and cannot reproduce the hydrothermal signal around the Central Indian Ridge segment. The overestimation of surface dFe concentration under the high-dust region at 10°N could indicate the potential role of scavenging by lithogenic particles as suggested by Ye and Völker (2017) for the tropical Atlantic Ocean. Comparing the five model runs in Figure 4, it is clear that the release of ligand and dFe from organic particles is important to form the dFe maximum. When the ligand is decoupled from the particle remineralization (*constL* run), the subsurface dFe maximum disappears entirely (Figure 4c). When the dissolution of organic scavenged Fe is suppressed (*No Fe rediss.* run), this dFe maximum is significantly reduced in magnitude and extension (Figure 4d). In contrast, the sedimentary Fe flux has a moderate impact only (Figure 4e). Also, the hydrothermal flux has little effect on the dFe distribution in this transect (Figure 4f).

3.2. Pacific Ocean

The GP02 transect maps the zonal dFe distribution in the North Pacific Ocean (Nishioka et al., 2013; Figures 5a and 5b). In this transect, there are several model biases. Our model exhibits the high dFe concentration around 800 m extending from west to east along the transect (Figures 5a and 5b), but this feature is more zonally elongated than observation. Observations indicate a strong subsurface Fe source in the western Pacific, which is underestimated in the model. The surface dFe concentration is overestimated by 0.4 nM, whereas the deep dFe concentration (at > 3,000 m) is significantly underestimated. The widespread overestimation of surface dFe comes from the upwelling of rich-dFe subsurface waters, which receive high dFe from the continental shelves. This may imply a weak scavenging rate or biases in the factors limiting the biological uptake, potentially related to the colimitation of productivity by macronutrient and Fe (Ingall et al., 2013).

Despite these biases, processes controlling the simulated subsurface dFe maximum at about 800 m are explored through four sensitivity experiments (*Full*, *ConstL*, *No Fe redissolution*, *Weak sed*, and *Weak hydro* runs). When the nonuniform ligand is suppressed in the (*constL*) run, this dFe maximum disappears entirely (Figure 5c). It is also greatly decreased in magnitude when the dFe sediment flux is decreased (*Weak sed* run, Figure 5e). On the contrary, dFe supply from the remineralization of scavenged Fe and hydrothermal vents seems to play only a small part (Figures 5d and 5f). This result is consistent with results of a recent observational study (Nishioka & Obata, 2017), suggesting that the high dFe concentration at middepth may come from the sedimentary Fe source. The model bias at this depth range could come from biases in the sedimentary Fe flux parameterization, which includes significant uncertainty.

The GP13 maps the zonal dFe distribution in the south western Pacific Ocean. The model reproduces several features of the dFe distribution in this region (Figures 6a and 6b). In particular, the model captures the elevated dFe concentration around 600–1,000 m from 160°E to 170°E. Moreover, the model reproduces low-surface dFe concentration observed across the transect. The strong zonal gradient of subsurface dFe concentration ~175°W is reproduced in the model. However, the pattern of subsurface dFe extreme is more horizontally and vertically compressed than observed.

The elevated dFe centered around ~175°E disappears when the nonuniform pattern of ligand is suppressed (Figure 6c) and is greatly decreased in magnitude and extension when the dFe hydrothermal flux is reduced (Figure 6f). On the other hand, this feature is only slightly decreased when the release of scavenged Fe associated with organic particles or the dFe supply from continental shelves is decreased (Figure 6de). Thus, our result, along with several observational studies (Ellwood et al., 2018; Fitzsimmons et al., 2014; Resing et al., 2015), confirms the role of the long-range transport (thousands of kilometers) of hydrothermal dFe from the southern East Pacific Rise to the dFe distribution in the upper 1,000 m of the South Pacific Ocean. In addition, our model result suggests that this transport is facilitated by the existence of a nonuniform, remineralized ligand class, protecting dFe from scavenging along the transport pathway. The GP16 section maps the zonal dFe distribution across the subtropical South Pacific Ocean (Resing et al., 2015; Figures 7a and 7b). In this transect, the model captures the low dFe concentration at the surface, which is a typical feature for the high-nutrient low-chlorophyll region (Figures 7a and 7b). However, the subsurface dFe maximum observed over almost
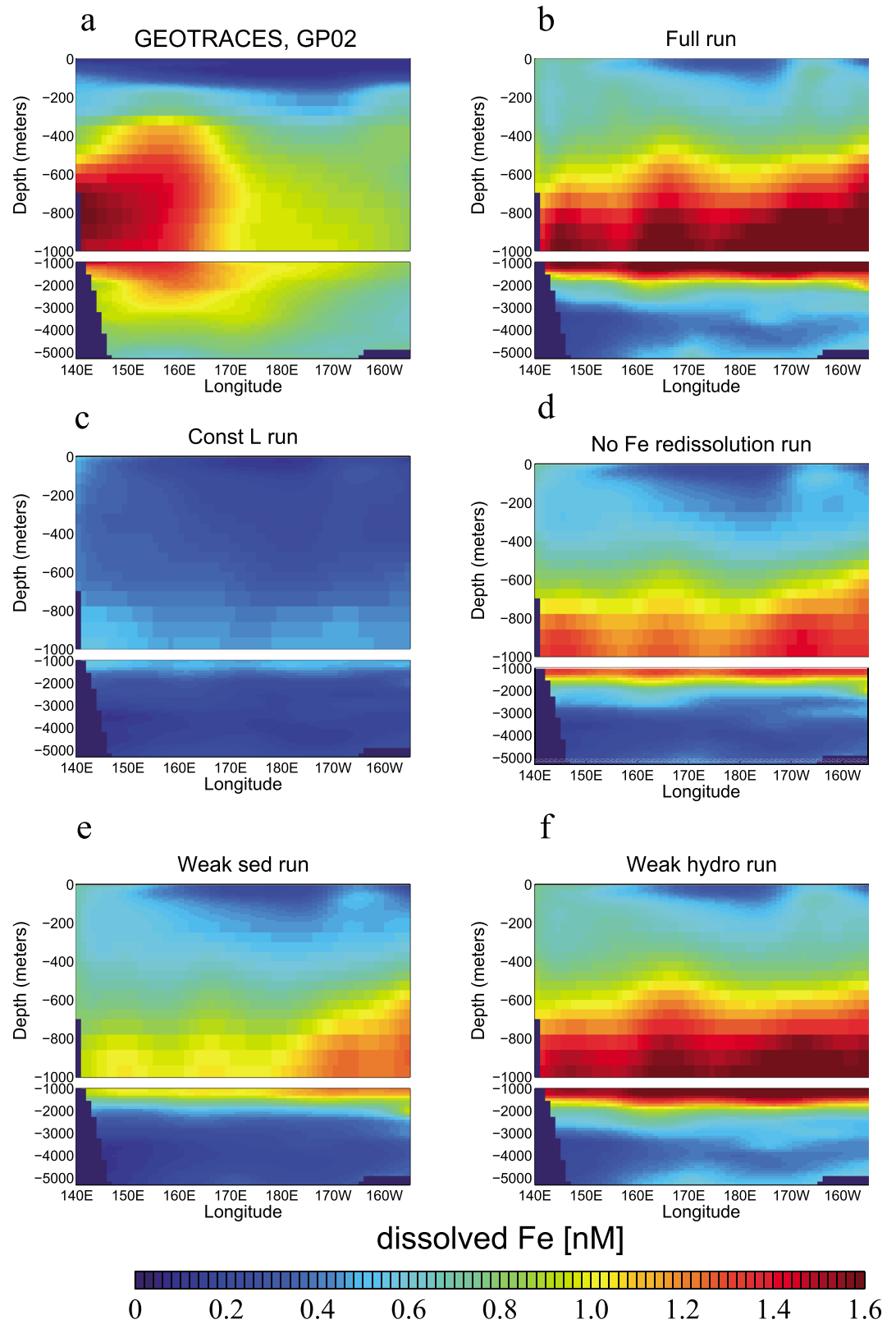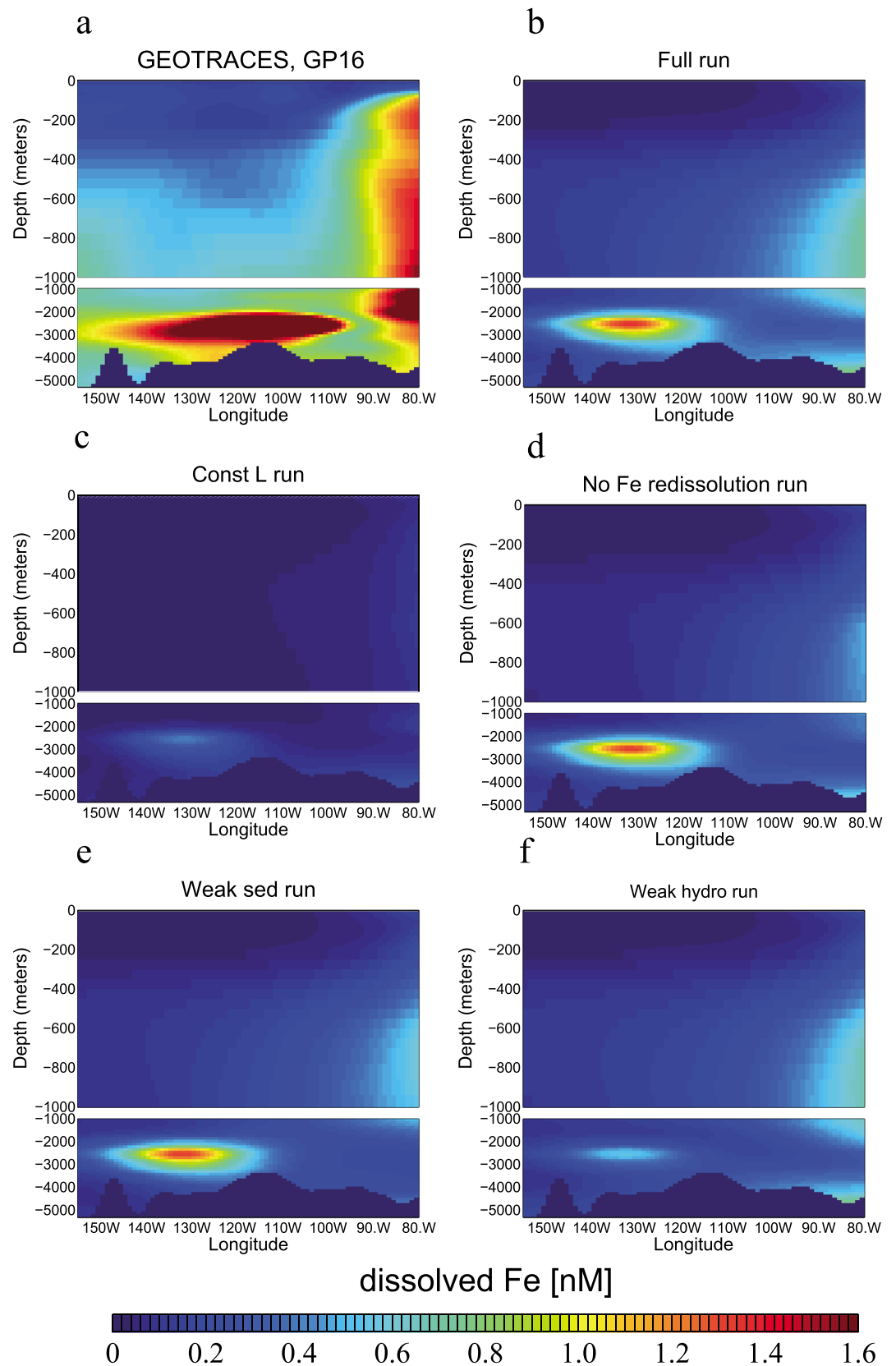
Figure 5. dFe distribution along the GP02 transect: (a) observations, (b) *Full* run, (c) *ConstL* run, (d)*No Fe redissolution* run, (e) *Weak sed* run, and (f) *Weak hydro* run. dFe = dissolved Fe.
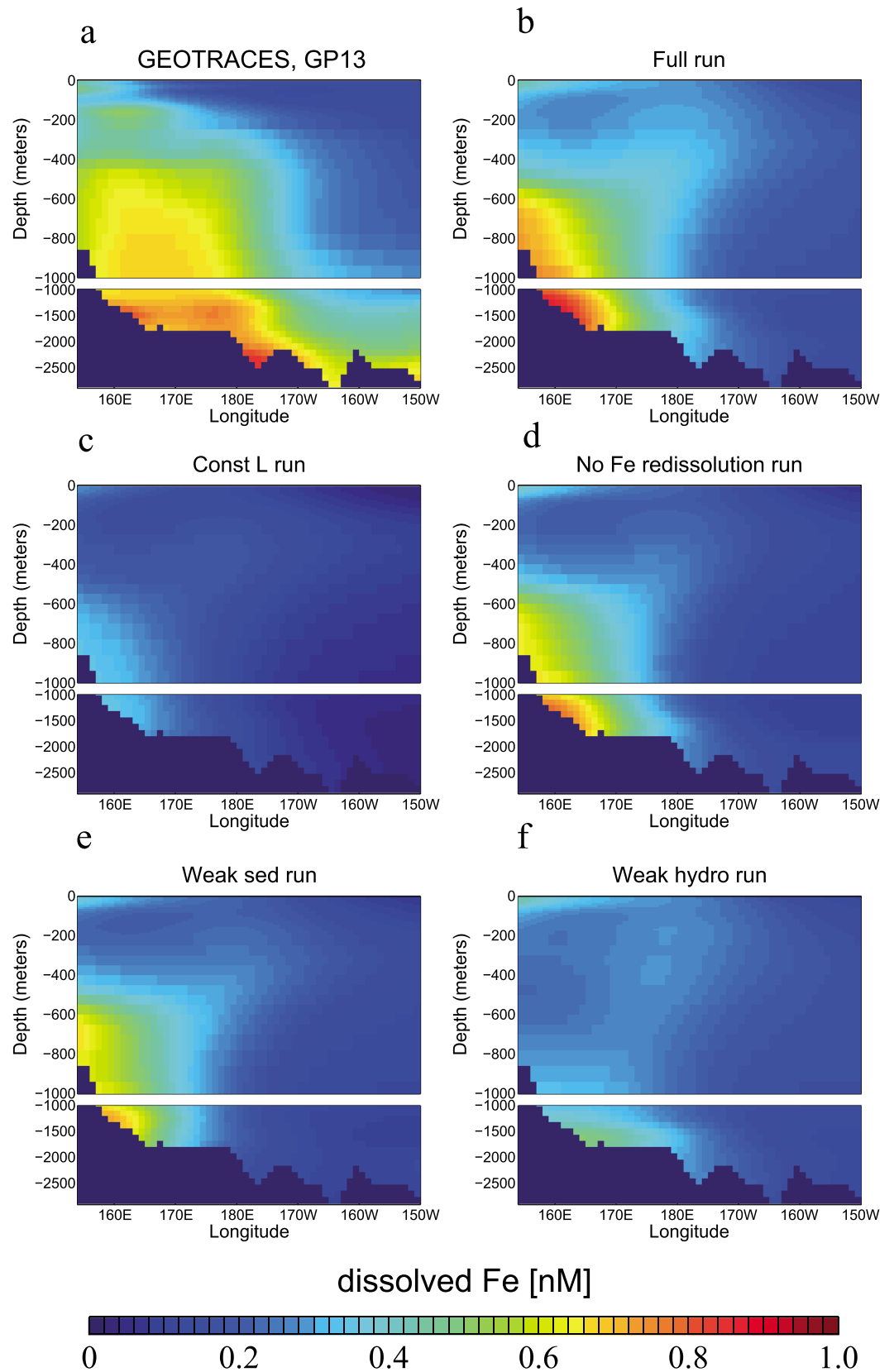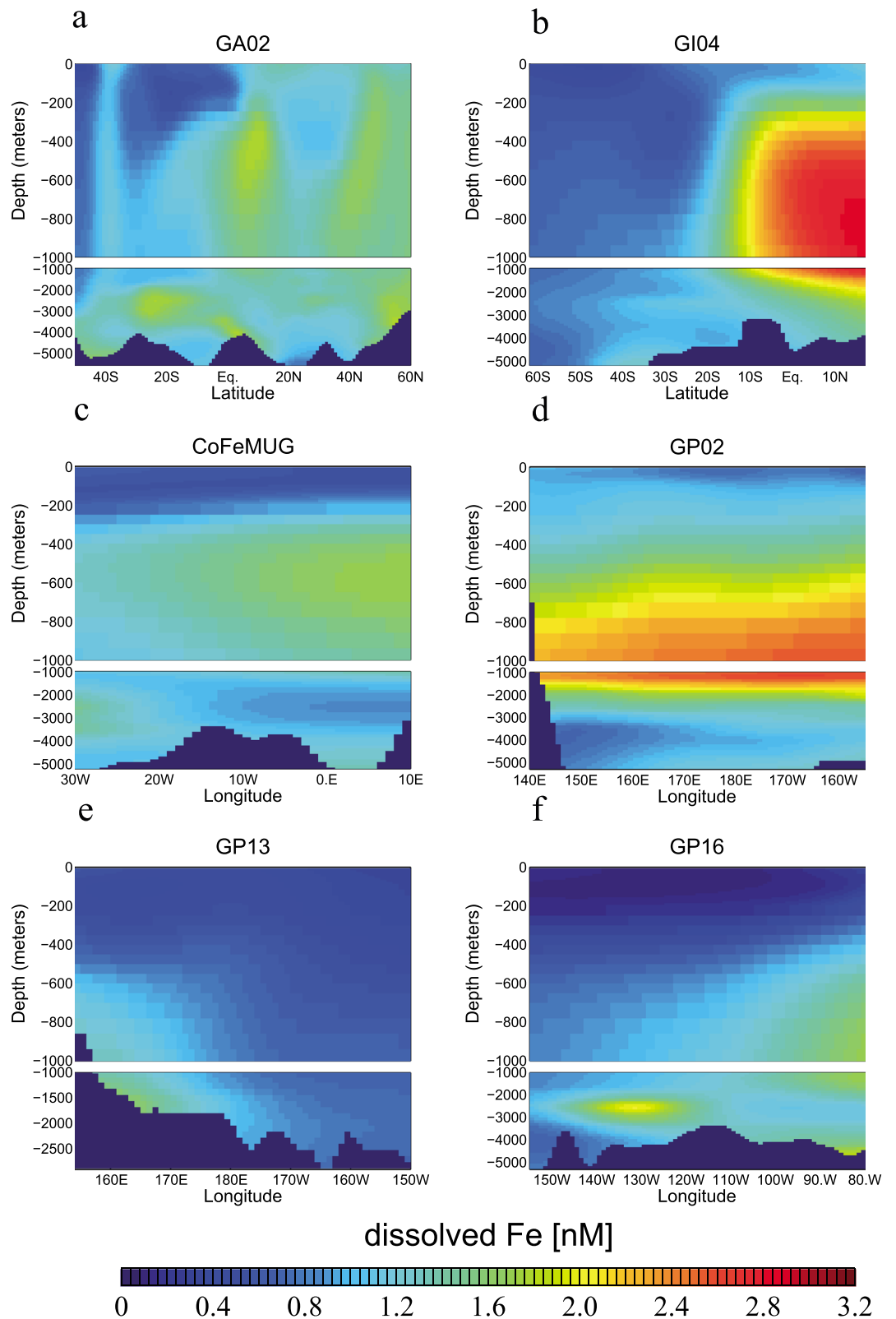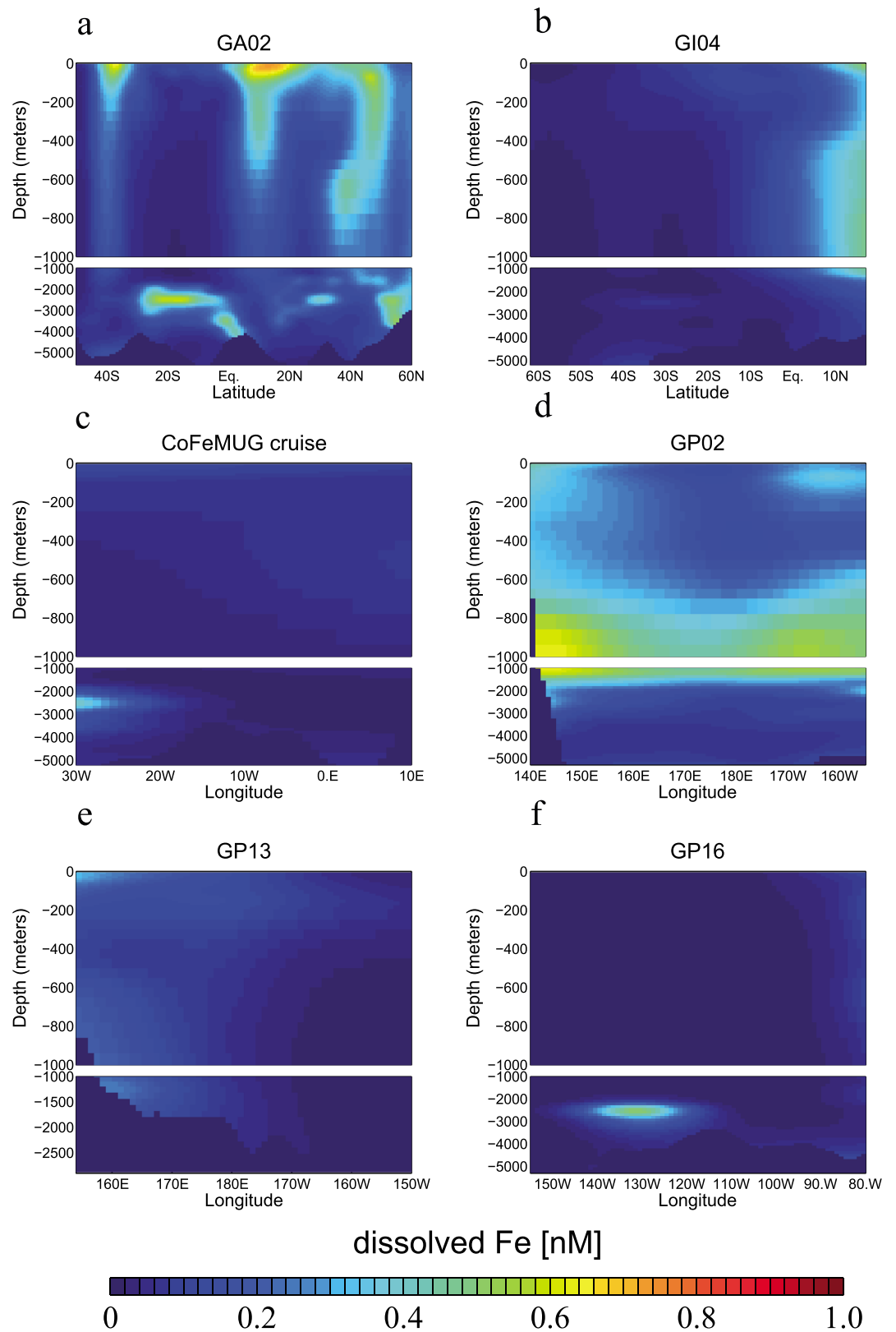
Figure 6. dFe distribution along the GP13 transect: (a) observations, (b) *Full* run, (c) *ConstL* run, (d) *No Fe redissolution* run, (e) *Weak sed* run, and (f) *Weak hydro* run. dFe = dissolved Fe.

Figure 7. dFe distribution along the GP16 transect: (a) observations, (b) *Full* run, (c) *ConstL* run, (d) *No Fe redissolution* run, (e) *Weak sed* run, and (f) *Weak hydro* run. dFe = dissolved Fe.

Figure 8. Modeled dFe distribution along the GEOTRACES transects from the *constK_L* run: (a) GA02, (b) GI04 (c) CoFeMUG, (d) GP02, (e) GP13, and (f) GP16. dFe = dissolved Fe.

Figure 9. Modeled dFe distribution along the GEOTRACES transects from the *Large* ΔK_L run: (a) GA02, (b) GI04 (c) CoFeMUG, (d) GP02, (e) GP13, and (f) GP16. dFe = dissolved Fe.

the entire water column (from 200 m to the bottom) in the eastern margin is greatly underestimated by the model. The model bias in this region is consistent with many other models analyzed in Tagliabue et al. (2016). Our model only shows a weak signal of this feature around 800–1,000 m with the concentration of 0.8 nM, about a half of the observation. This signal disappeared in three sensitivity experiments: *ConstL*, *No Fe rediss.*, and *Weak sed* (Figures 7c–7e). A recent observational study argued that this maximum could be a signal of a very persistent dFe flux from resuspended sediments (John et al., 2017). Furthermore, the observed hydrothermal signal around 3,000 m at 110°W is displaced westward and greatly underestimated in our model. This hydrothermal signal is decreased in the model when a lower dFe/^{3}He ratio from Tagliabue et al. (2010) is applied (Figure 7f).

Summarizing the results so far, the model-data comparison showed some strengths and weaknesses in reproducing the observed dFe distribution. The model was able to reproduce the general pattern and magnitude of the subsurface dFe maxima in many sections (GA02, CoFeMUG, GI04, and GP13), but it also showed significant model biases in other sections (GP02 and GP16). Sensitivity runs showed the relative importance of different Fe sources in reproducing the observation and implied some potential causes for model biases. For deep waters, the hydrothermal vents are the most important Fe source. Thus, mismatches in the deep ocean between model and observed dFe concentration likely originate from biases in the model parameterization of hydrothermal dFe source. The middepth dFe in the GA02, CoFeMUG, and GI04 transects is particularly sensitive to the remineralization of scavenged Fe associated with the sinking organic particles. In contrast, the middepth dFe is sensitive to sedimentary dFe sources in GP02 and GP16 and to hydrothermal dFe inputs in GP13. Sensitivity experiments also revealed the important role of the nonuniform distribution of organic ligands in all of the sections. Elevated ligand concentration in the middepth water column plays a crucial role in the retention of dFe. Additional sensitivity experiments (*constK$_L$* and *Large ΔK$_L$*) are performed to examine the importance of different types of ligands.

4. The Sensitivity of DFE Distribution to the Ligand Binding Strength

Two sensitivity experiments are specifically designed to examine the role of ligands' binding strengths in controlling the dFe distribution. The *constK$_L$* run sets the two conditional stability constants to be at the intermediate value, $10^{11.5}$ mol/L. The *Large ΔK$_L$* run does the opposite, making the difference between these two values greater (10^{13} mol/L for L_1 and 10^{10} mol/L for L_2). Again, the models are spun up for 1,000 years to reach a new steady state, and the results are displayed in Figures 8 and 9.

Due to the large increase in the dFe values, Figure 8 uses a different color bar relative to the six previous figures. Below the surface waters, the organic ligand is dominated by the L_2 ligand. In the *constK$_L$* run, the binding strength of the subsurface ligand L_2 is increased by a factor of 3 (from 10^{11} to $10^{11.5}$ mol/L). In response, the amplitude of the subsurface dFe maxima increases by about factor of 2 in the model. This leads to an increase in the surface ocean dFe concentration even though the surface ligand class L_1 is decreased from 10^{12} to $10^{11.5}$ mol/L. This is caused by the vertical supply of subsurface-elevated dFe concentration to the surface waters via vertical mixing and upwelling (Tagliabue, Sallee, et al., 2014). This result indicates the prominent role of L_2 in the retention of dFe throughout the water column, thus increasing the binding strength of L_2 that caused a widespread overestimation of dFe in all of the transects.

Figure 9 shows the results from the *Large ΔK$_L$* run. In this case, the binding strength of the subsurface ligand L_2 decreases by a factor of 10 (from 10^{11} to 10^{10} mol/L), and the global dFe concentration in general decreases by a factor of 5. Figure 9 uses a different color bar relative to the previous figures because of the low dFe concentrations. Despite the increase in L_1 (from 10^{12} to 10^{13} mol/L), the overall dFe concentration in the water column is controlled by the binding strength of L_2. More importantly, all the observed GEOTRACES dFe maxima disappeared or are greatly reduced in magnitude in the *Large ΔK$_L$* run. These results highlight the crucial role of the subsurface ligand class in maintaining middepth dFe maxima.

5. Discussion and Conclusion

The GEOTRACES program (Anderson et al., 2014; Henderson et al., 2007; Mawji et al., 2015) has significantly increased the data coverage for dFe and ligands in the global oceans, providing a unique opportunity to test ocean biogeochemistry models and improve the representation of biogeochemical processes essential for the Fe cycling (Tagliabue et al., 2016, Völker & Tagliabue, 2015). While there have been significant advances
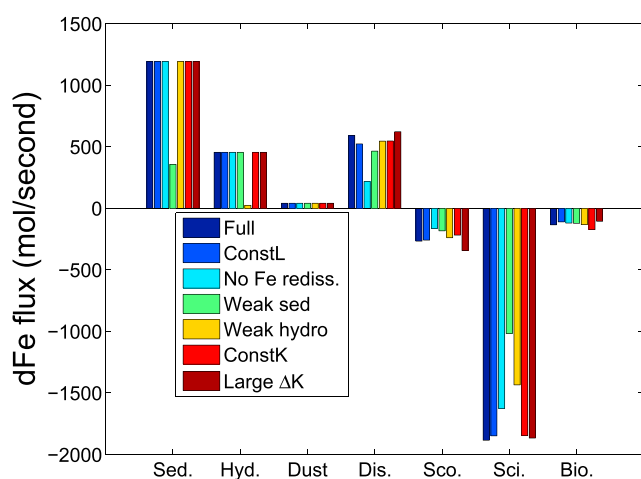
Figure 10. The globally integrated sources and sinks of dFe from each of the model runs. "Sed" is the shelf sediment, and "hyd" is for hydrothermal source. "dis" is for release of dFe from remineralization and desorption, and "sco" and "sci" are the scavenging onto organic and inorganic particles respectively. "bio" is for the loss of Fe due to the biological uptake. dFe = dissolved Fe.

in the understanding and modeling capability of the Fe cycling in the last decade, the new observations revealed that there are many features of dFe distribution that are still missing or heavily biased in the current generation of models (Tagliabue et al., 2016). Motivated by the newly available data set, we explored the processes driving the observed ocean dFe distribution by a suite of sensitivity experiments in an ocean biogeochemistry model with a refined parameterization for the Fe cycling. Specifically, our model includes three external dFe sources, which are modified from previous studies (Dutkiewicz et al., 2015; Moore & Braucher, 2008) to better reproduce the observations, and an improved ligand parameterization. Our ligand parameterization considers two spatially varying ligand classes, which have different binding strengths. Their distributions are parameterized as functions of DOC and AOU. The empirical constants in the ligand parameterizations are calibrated to fit the observed ligand distribution in the least squares sense. While these parameterization themselves are not new and have some limitations (Gledhill & Buck, 2012; Velasquez et al., 2016), the simplicity of this approach allows us to determine the underlying mechanisms in a clear way.

Even though our model still has several biases when compared with observation, it starts capturing some major features such as the subsurface dFe maxima observed in various GEOTRACES transects in different ocean basins (Noble et al., 2012; Nishioka et al., 2013; Nishioka & Obata, 2017; Rijkenberg et al., 2014; Resing et al., 2015) and provided an improved understanding of the mechanisms behind them. In particular, we examined the relative roles of the release of scavenged Fe back to the water column via the remineralization of sinking organic particles (Boyd et al., 2010; Velasquez et al., 2016) and of the external dFe supply from continental shelves and hydrothermal vents. The former process turned out to be the crucial mechanism behind the subsurface dFe maxima in the thermocline of high-dust regions. In the surface of the tropical Atlantic and Indian Oceans, the deposited dust Fe is mostly scavenged onto organic particles, which then sink and remineralize at middepth water column. In addition, the nonuniform distribution of relatively weaker L_2 ligand was found to be the key factor for maintaining the subsurface dFe maxima in the model. Parameterizing the L_2 ligand using the AOU distribution was crucial to improve dFe distribution by representing the particle remineralization as a source of the ligand. Similar results are reported in Tagliabue et al. (2016), who showed that the inclusion of the particle remineralization source for ligand in ocean biogeochemistry models improves the reproduction of the subsurface dFe maxima. Earlier models (P05, D05, and Tagliabue et al., 2016) that applied a uniform constant ligand and neglected the dissolution of scavenged Fe did not reproduce the observed subsurface dFe maxima. When the release of either scavenged Fe or ligand from [c1] sinking organic particles is suppressed, the subsurface dFe maxima observed in the Indian Ocean and Atlantic Ocean transects are either disappeared or greatly reduced in magnitude in the model. Thus, in high-dust regions of the Indian and Atlantic basins, the simultaneous release of ligand and scavenged Fe from organic particles not only supplies dFe to the subsurface waters but also protects dFe from being scavenged, maintaining a high level of subsurface dFe concentration. In fact, the model tends to overestimate the surface dFe in high-dust regions and likely indicates bias in the representation of processes that remove dFe where dust deposition is high (Ye & Völker, 2017). This bias may reflect the missing colloidal pumping mechanism for dFe loss in our model, which could be important for high dust deposition regions (Fitzsimmons et al., 2015).

The Fe sources from the continental shelves and hydrothermal vents are found to be the important sources of the subsurface dFe maxima in the thermocline of low-dust regions in the Pacific Ocean. The particle-remineralized ligand is also important in sustaining the subsurface dFe maxima in these regions, but the dFe supply from organic particles seems to be less important than from external sources. In the deep waters, the model still shows several biases including the tendency to underestimate deep dFe concentration and to displace the dFe hydrothermal signals. The underestimation of hydrothermal Fe can be addressed by increasing the dFe/^{3}He ratio relative to the value suggested by Tagliabue et al. (2010) and using different ratios for different ocean basins. However, the spatial biases indicate potential biases in the source regions of the hydrothermal dFe and how it is transported in the deep ocean.

Figure 10 shows the dFe sources and sinks from all of the experiments. In terms of the external Fe sources, the hydrothermal and sedimentary Fe sources dominate the Fe input into the ocean. The largest removal mechanism is the scavenging onto inorganic particles, which is partially mediated by the release of Fe by remineralization and desorption.

When the external Fe input is reduced in *Weak sed* and *Weak hydro* runs, the removal of Fe by the inorganic scavenging is also reduced, thus balancing the input and output on the global scale. In these simulations, dFe maxima in high-dust regions seem to be only slightly decreased, reflecting the dominance of the atmospheric deposition and internal cycling processes in these regions.

When the dissolution of organic scavenged Fe is turned off (*No Fe rediss* run), the remineralization and desorption source of Fe is diminished in the global budget. However, the subsurface dFe maxima in the Pacific basin (GP13 and GP02) were not significantly affected in this run, reflecting the dominance of external inputs, in particular, the sedimentary and hydrothermal sources. Given the potential role of the subsurface dFe as a source for Fe-limited upwelling regions (Tagliabue, Sallee, et al., 2014), these external sources can have far-reaching effects on the marine ecosystems and the biological carbon pumps.

The sensitivity experiments with altered ligand parameterizations showed that the global dFe budget and distribution are sensitive to the strength and concentration of the subsurface ligand. When the binding strength of this ligand class increases/decreases, the global mean dFe concentration is increased/decreased. In particular, when the binding strength is reduced, almost all the middepth dFe maxima disappeared in the model. The impact of the siderophores-type surface ligand seems to be negligible in controlling the subsurface dFe maxima and the global dFe budget in general. These effects are best seen by looking at the change of dFe concentration in ocean transects but not as clear when examining the global dFe budget (Figure 10). These results suggest that the uncertainty in the binding strength of L_2 ligand class has a big implication on the dFe cycling.

Finally, this study owes its existence to the hard work of the scientific community who joined the efforts to produce high-quality measurements of trace metal elements and associated biogeochemical variables across the global oceans. In this light, it is critical to maintain the observing capabilities and to develop an improved understanding of the mechanisms driving the ocean's trace metal cycling and its impact on the ecosystem and biogeochemical cycling.

References

Adly, C. L., Tremblay, J. E., Powell, R. T., Armstrong, E., Peers, G., & Price, N. M. (2015). Response of heterotrophic bacteria in a mesoscale iron enrichment in the northeast subarctic Pacific Ocean. *Limnology and Oceanography*, *60*(1), 136–148. https://doi.org/10.1002/lno.10013

Anderson, R. F., Cheng, H., Edwards, R. L., Fleisher, M. Q., Hayes, C. T., Huang, K. F., et al. (2016). How well can we quantify dust deposition to the ocean?, Philosophical transactions of the royal society A: Mathematical. *Physical and Engineering Sciences*, *374*(2081), 20150285. https://doi.org/10.1098/rsta.2015.0285

Anderson, R. F., MAwji, E., Cutter, G. A., Measures, C. I., & Jeandel, C. (2014). Geotraces: Changing the way we explore ocean chemistry. *Oceanography*, *27*(1), 50–61.

Archer, D. E., & Johnson, K. (2000). A model of the iron cycle in the ocean. *Global Biogeochemical Cycles*, *14*(1), 269–279. https://doi.org/10.1029/1999GB900053

Barbeau, K., Rue, E. L., Bruland, K. W., & Butler, A. (2001). Photochemical cycling of iron in the surface ocean mediated by microbial iron(III)-binding ligands. *Nature*, *413*(6854), 409–413.

Behrenfeld, M. J., & Falkowski, P. G. (1997). A consumer's guide to phytoplankton primary productivity models. *Limnology and Oceanography*, *42*(7), 1479–1491. https://doi.org/10.4319/lo.1997.42.7.1479

Boiteau, R. M., & Repeta, D. J. (2015). An extended siderophore suite from synechococcus sp. PCC 7002 revealed by LC-ICPMS-ESIMS. *Metallomics*, *7*(5), 877–884. https://doi.org/10.1039/C5MT00005J

Boyd, P. W., & Ellwood, M. J. (2010). The biogeochemical cycle of iron in the ocean. *Nature Geoscience*, *3*(10), 675–682. https://doi.org/10.1038/ngeo964

Boyd, P. W., Ibisanmi, E., Sander, S. G., Hunter, K. A., & Jackson, G. A. (2010). Remineralization of upper ocean particles: Implications for iron biogeochemistry. *Limnology and Oceanography*, *55*(3), 1271–1288. https://doi.org/10.4319/lo.2010.55.3.1271

Boyd, P. W., Watson, A. J., Law, C. S., Abraham, E. R., Trull, T., Murdoch, R., et al. (2000). A mesoscale phytoplankton bloom in the polar Southern Ocean stimulated by iron fertilization. *Nature*, *407*(6805), 695–702.

Buck, K. N., Selph, K. E., & Barbeau, K. A. (2010). Iron-binding ligand production and copper speciation in an incubation experiment of Antarctic Peninsula shelf waters from the Bransfield Strait, Southern Ocean. *Marine Chemistry*, *122*(1-4), 148–159. https://doi.org/10.1016/j.marchem.2010.06.002

Buck, K. N., Sohst, B., & Sedwick, P. N. (2015). The organic complexation of dissolved iron along the U.S. GEOTRACES (GA03) North Atlantic Section. *Deep Sea Research Part II: Topical Studies in Oceanography*, *116*, 152–165. https://doi.org/10.1016/j.dsr2.2014.11.016

Duce, R. A., & Tindale, N. W. (1991). Atmospheric transport of iron and its deposition in the ocean. *Limnology and Oceanography*, *36*(8), 1715–1726. https://doi.org/10.4319/lo.1991.36.8.1715

Dutay, J. C., Tagliabue, A., Kriest, I., & van Hulten, M. M. P. (2015). Modelling the role of marine particle on large scale 231pa, 230th, iron and aluminium distributions. *Progress in Oceanography*, *133*, 66–72. https://doi.org/10.1016/j.pocean.2015.01.010

Dutkiewicz, S., Follows, M. J., & Parekh, P. (2005). Interactions of the iron and phosphorus cycles: A three-dimensional model study. *Global Biogeochemical Cycles*, *19*, GB1021. https://doi.org/10.1029/2004GB002342

Dutkiewicz, S., Hickman, A. E., Jahn, O., Gregg, W. W., Mouw, C. B., & Follows, M. J. (2015). Capturing optically important constituents and properties in a marine biogeochemical and ecosystem model. *Biogeosciences*, *12*(14), 4447–4481. https://doi.org/10.5194/bg-12-4447-2015

Ellwood, M. J., Bowie, A. R., Baker, A., Gault-Ringold, M., Hassler, C., Law, C. S., et al. (2018). Insights into the biogeochemical cycling of iron, nitrate, and phosphate across a 5,300 km South Pacific zonal section (153°E–150°W). *Global Biogeochemical Cycles*, *32*, 187–Ű207. https://doi.org/10.1002/2017GB005736

Elrod, V. A., Berelson, W. M., Coale, K. H., & Johnson, K. S. (2004). The flux of iron from continental shelf sediments: A missing source for global budgets. *Geophysical Research Letters*, *31*, L12307. https://doi.org/10.1029/2004GL020216

Fitzsimmons, J. N., Boyle, E. A., & Jenkins, W. J. (2014). Distal transport of dissolved hydrothermal iron in the deep South Pacific Ocean. *Proceedings of the National Academy of Sciences*, *111*(47), 16,654–16,661. https://doi.org/10.1073/pnas.1418778111

Fitzsimmons, J. N., Carrasco, G. G., Wu, J., Roshan, S., Hatta, M., Measures, C. I., et al. (2015). Partitioning of dissolved iron and iron isotopes into soluble and colloidal phases along the GA03 GEOTRACES North Atlantic Transect. *Deep Sea Research Part II: Topical Studies in Oceanography*, *116*, 130–151. https://doi.org/10.1016/j.dsr2.2014.11.014

Fowler, S. W., & Knauer, G. A. (1986). Role of large particles in the transport of elements and organic compounds through the oceanic water column. *Progress in Oceanography*, *16*(3), 147–194. https://doi.org/10.1016/0079-6611(86)90032-7

Galbraith, E. D., Gnanadesikan, A., Dunne, J. P., & Hiscock, M. R. (2010). Regional impacts of iron-light colimitation in a global biogeochemical model. *Biogeosciences*, *7*(3), 1043–1064. https://doi.org/10.5194/bg-7-1043-2010

Garcia, H. E., & Gordon, L. I. (1992). Oxygen solubility in seawater: Better fitting equations. *Limnology and Oceanography*, *37*(6), 1307–1312. https://doi.org/10.4319/lo.1992.37.6.1307

Gent, P. R., & Mcwilliams, J. C. (1990). Isopycnal mixing in ocean circulation models. *Journal of Physical Oceanography*, *20*(1), 150–155. https://doi.org/10.1175/1520-0485(1990)020<0150:imiocm>2.0.co;2

Gerringa, L. J. A., Rijkenberg, M. J. A., Schoemann, V., Laan, P., & de Baar, H. J. W. (2015). Organic complexation of iron in the West Atlantic Ocean. *Marine Chemistry*, *177*(Part 3), 434–446. https://doi.org/10.1016/j.marchem.2015.04.007

Gledhill, M., & Buck, K. (2012). The organic complexation of iron in the marine environment: A review. *Frontiers in Microbiology*, *3*(69). https://doi.org/10.3389/fmicb.2012.00069

Hassler, C. S., Schoemann, V., Nichols, C. M., Butler, E. C. V., & Boyd, P. W. (2011). Saccharides enhance iron bioavailability to Southern Ocean phytoplankton. *Proceedings of the National Academy of Sciences*, *108*(3), 1076–1081. https://doi.org/10.1073/pnas.1010963108

Hassler, C., van den Berg, C., & Boyd, P. (2017). Towards a regional classification to provide a more inclusive examination of the ocean biogeochemistry of iron-binding ligands. *Frontiers in Marine Science*, *4*(19). https://doi.org/10.3389/fmars.2017.00019

Henderson, G., Anderson, R. F., Adkins, J., Andersson, E., Boyle, P., Cutter, G. A., et al. (2007). Geotraces—An international study of the global marine biogeochemical cycles of trace elements and their isotopes. *Chemie der Erde - Geochemistry*, *67*(2), 85–131. https://doi.org/10.1016/j.chemer.2007.02.001

Honeyman, B. D., Balistrieri, L. S., & Murray, J. W. (1988). Oceanic trace metal scavenging: The importance of particle concentration, deep sea research part A. *Oceanographic Research Papers*, *35*(2), 227–246. https://doi.org/10.1016/0198-0149(88)90038-6

Honeyman, B. D., & Santschi, P. H. (1989). A Brownian-pumping model for oceanic trace metal scavenging: Evidence from Th isotopes. *Journal of Marine Research*, *47*(4), 951–992. https://doi.org/10.1357/002224089785076091

Hunter, K. A., & Boyd, P. W. (2007). Iron-binding ligands and their role in the ocean biogeochemistry of iron. *Environmental Chemistry*, *4*(4), 221–232. https://doi.org/10.1071/EN07012

Hutchins, D. A., & Boyd, P. W. (2016). Marine phytoplankton and the changing ocean iron cycle. *Nature Climate Change*, *6*(12), 1072–1079. https://doi.org/10.1038/nclimate3147

Ingall, E. D., Diaz, J. M., Longo, A. F., Oakes, M., Finney, L., Vogt, S., et al. (2013). Role of biogenic silica in the removal of iron from the Antarctic seas. *Nature Communications*, *4*, 1981. https://doi.org/10.1038/ncomms2981

Ito, T., Nenes, A., Johnson, M. S., Meskhidze, N., & Deutsch, C. (2016). Acceleration of oxygen decline in the tropical Pacific over the past decades by aerosol pollutants. *Nature Geoscience*, *9*(6), 443–447. https://doi.org/10.1038/ngeo2717

Jackson, G. A., & Burd, A. B. (2015). Simulating aggregate dynamics in ocean biogeochemical models. *Progress in Oceanography*, *133*, 55–65. https://doi.org/10.1016/j.pocean.2014.08.014

Jeandel, C., Rutgers van der Loeff, M., Lam, P. J., Roy-Barman, M., Sherrell, R. M., Kretschmer, S., et al. (2015). What did we learn about ocean particle dynamics in the GEOSECS—JGOFS era? *Progress in Oceanography*, *133*, 6–16. https://doi.org/10.1016/j.pocean.2014.12.018

Jickells, T. D., An, Z. S., Andersen, K. K., Baker, A. R., Bergametti, G., Brooks, N., et al. (2005). Global iron connections between desert dust, ocean biogeochemistry, and climate. *Science*, *308*(5718), 67–71. https://doi.org/10.1126/science.1105959

John, S. G., Helgoe, J., Townsend, E., Weber, T., DeVries, T., Tagliabue, A., et al. (2017). *Biogeochemical cycling of Fe and Fe stable isotopes in the Eastern Tropical South Pacific* (Vol. 201, pp. 66–76). https://doi.org/10.1016/j.marchem.2017.06.003

Johnson, K. S., Chavez, F. P., & Friederich, G. E. (1999). Continental-shelf sediment as a primary source of iron for coastal phytoplankton. *Nature*, *398*(6729), 697–700.

Johnson, K. S., Gordon, R. M., & Coale, K. H. (1997). What controls dissolved iron concentrations in the world ocean? *Marine Chemistry*, *57*(3), 137–161. https://doi.org/10.1016/S0304-4203(97)00043-1

Johnson, M. S., & Meskhidze, N. (2013). Atmospheric dissolved iron deposition to the global oceans: Effects of oxalate-promoted fe dissolution, photochemical redox cycling, and dust mineralogy. *Geoscientific Model Development*, *6*(4), 1137–1155. https://doi.org/10.5194/gmd-6-1137-2013

Kustka, A. B., Jones, B. M., Hatta, M., Field, M. P., & Milligan, A. J. (2015). The influence of iron and siderophores on eukaryotic phytoplankton growth rates and community composition in the Ross Sea. *Marine Chemistry*, *173*, 195–207. https://doi.org/10.1016/j.marchem.2014.12.002

Laglera, L. M., & van den Berg, C. M. G. (2009). Evidence for geochemical control of iron by humic substances in seawater. *Limnology and Oceanography*, *54*(2), 610–619. https://doi.org/10.4319/lo.2009.54.2.0610

Large, W. G., McWilliams, J. C., & Doney, S. C. (1994). Oceanic vertical mixing: A review and a model with a nonlocal boundary layer parameterization. *Reviews of Geophysics*, *32*(4), 363–403. https://doi.org/10.1029/94RG01872

Laws, E. A., D'Sa, E., & Naik, P. (2011). Simple equations to estimate ratios of new or export production to total production from satellite-derived estimates of sea surface temperature and primary production. *Limnology and Oceanography: Methods*, *9*(12), 593–601. https://doi.org/10.4319/lom.2011.9.593

Liu, X., & Millero, F. J. (2002). The solubility of iron in seawater. *Marine Chemistry*, *77*(1), 43–54. https://doi.org/10.1016/S0304-4203(01)00074-3

Macrellis, H. M., Trick, C. G., Rue, E. L., Smith, G., & Bruland, K. W. (2001). Collection and detection of natural iron-binding ligands from seawater. *Marine Chemistry*, *76*(3), 175–187. https://doi.org/10.1016/S0304-4203(01)00061-5

Mahowald, N. M., Engelstaedter, S., Luo, C., Sealy, A., Artaxo, P., Benitez-Nelson, C., et al. (2009). Atmospheric iron deposition: Global distribution, variability, and human perturbations. *Annual Review of Marine Science*, *1*(1), 245–278. https://doi.org/10.1146/annurev.marine.010908.163727

Marshall, J., Adcroft, A., Hill, C., Perelman, L., & Heisey, C. (1997). A finite-volume, incompressible Navier Stokes model for studies of the ocean on parallel computers. *Journal of Geophysical Research*, *102*(C3), 5753–5766. https://doi.org/10.1029/96JC02775

Marshall, J., Hill, C., Perelman, L., & Adcroft, A. (1997). Hydrostatic, quasi-hydrostatic, and nonhydrostatic ocean modeling. *Journal of Geophysical Research*, *102*(C3), 5733–5752. https://doi.org/10.1029/96JC02776

Martin, J. H., Knauer, G. A., Karl, D. M., & Broenkow, W. W. (1987). Vertex: Carbon cycling in the northeast pacific, deep sea research part A. *Oceanographic Research Papers*, *34*(2), 267–285. https://doi.org/10.1016/0198-0149(87)90086-0

Mawji, E., Schlitzer, R., Dodas, E. M., Abadie, C., Abouchami, W., Anderson, R. F., et al. (2015). The GEOTRACES intermediate data product 2014. *Marine Chemistry*, *177*(Part 1), 1–8. https://doi.org/10.1016/j.marchem. 2015.04.005

Middag, R., van Hulten, M. M. P., Van Aken, H. M., Rijkenberg, M. J. A., Gerringa, L. J. A., Laan, P., & de Baar, H. J. W. (2015). Dissolved aluminium in the ocean conveyor of the West Atlantic Ocean: Effects of the biological cycle, scavenging, sediment resuspension and hydrography. *Marine Chemistry*, *177*(Part 1), 69–86. https://doi.org/10.1016/j.marchem.2015.02.015

Misumi, K., Lindsay, K., Moore, J. K., Doney, S. C., Tsumune, D., & Yoshida, Y. (2013). Humic substances may control dissolved iron distributions in the global ocean: Implications from numerical simulations. *Global Biogeochemical Cycles*, *27*, 450–462. https://doi.org/10.1002/gbc.20039

Moore, J. K., & Braucher, O. (2008). Sedimentary and mineral dust sources of dissolved iron to the world ocean. *Biogeosciences*, *5*(3), 631–656. https://doi.org/10.5194/bg-5-631-2008

Moore, C. M., Mills, M. M., Arrigo, K. R., Berman-Frank, I., Bopp, L., Boyd, P. W., et al. (2013). Processes and patterns of oceanic nutrient limitation. *Nature Geoscience*, *6*(9), 701–710. https://doi.org/10.1038/ngeo1765

Nishioka, J., & Obata, H. (2017). Dissolved iron distribution in the western and central subarctic Pacific: HNLC water formation and biogeochemical processes. *Limnology and Oceanography*, *62*(5), 2004–2022. https://doi.org/10.1002/lno. 10548

Nishioka, J., Obata, H., & Tsumune, D. (2013). Evidence of an extensive spread of hydrothermal dissolved iron in the Indian Ocean. *Earth and Planetary Science Letters*, *361*, 26–33. https://doi.org/10.1016/j.epsl.2012.11.040

Noble, A. E., Lamborg, C. H., Ohnemus, D. C., Lam, P. J., Goepfert, T. J., Measures, C. I., et al. (2012). Basin-scale inputs of cobalt, iron, and manganese from the Benguela-Angola front to the South Atlantic Ocean. *Limnology and Oceanography*, *57*(4), 989–1010. https://doi.org/10.4319/lo.2012.57.4.0989

Parekh, P., Follows, M. J., & Boyle, E. A. (2005). Decoupling of iron and phosphate in the global ocean. *Global Biogeochemical Cycles*, *19*, GB2020. https://doi.org/10.1029/2004GB002280

Redi, M. H. (1982). Oceanic isopycnal mixing by coordinate rotation. *Journal of Physical Oceanography*, *12*(10), 1154–1158. https://doi.org/10.1175/1520-0485(1982)012<1154:OIMBCR>2.0.CO;2

Resing, J. A., Sedwick, P. N., German, C. R., Jenkins, W. J., Moffett, J. W., Sohst, B. M., & Tagliabue, A. (2015). Basin-scale transport of hydrothermal dissolved metals across the South Pacific Ocean. *Nature*, *523*(7559), 200–203. https://doi.org/10.1038/nature14577

Revels, B. N., Ohnemus, D. C., Lam, P. J., Conway, T. M., & John, S. G. (2015). The isotopic signature and distribution of particulate iron in the North Atlantic Ocean. *Deep Sea Research Part II: Topical Studies in Oceanography*, *116*, 321–331. https://doi.org/10.1016/j.dsr2.2014.12.004

Rijkenberg, M. J. A., Middag, R., Laan, P., Gerringa, L. J. A., van Aken, H. M., Schoemann, V., et al. (2014). The distribution of dissolved iron in the West Atlantic Ocean. *PLoS One*, *9*(6), e101323. https://doi.org/10.1371/journal.pone.0101323

Rue, E. L., & Bruland, K. W. (1995). Complexation of iron(III) by natural organic ligands in the central North Pacific as determined by a new competitive ligand equilibration/adsorptive cathodic stripping voltammetric method. *Marine Chemistry*, *50*(1), 117–138. https://doi.org/10.1016/0304-4203(95)00031-L

Saito, M. A., Noble, A. E., Tagliabue, A., Goepfert, T. J., Lamborg, C. H., & Jenkins, J. (2013). Slow-spreading submarine ridges in the South Atlantic as a significant oceanic iron source. *Nature Geoscience*, *6*(9), 775–779. https://doi.org/10.1038/ngeo1893

Salt, L. A., van Heuven, S. M. A. C., Claus, M. E., Jones, E. M., & de Baar, H. J. W. (2015). Rapid acidification of mode and intermediate waters in the southwestern Atlantic Ocean. *Biogeosciences*, *12*(5), 1387–1401. https://doi.org/10.5194/bg-12-1387-2015

Sedwick, P. N., Church, T. M., Bowie, A. R., Marsay, C. M., Ussher, S. J., Achilles, K. M., et al. (2005). Iron in the Sargasso Sea (Bermuda Atlantic Time-series Study region) during summer: Eolian imprint, spatiotemporal variability, and ecological implications. *Global Biogeochemical Cycles*, *19*, GB4006. https://doi.org/10.1029/2004GB002445

Solomon, H. (1971). On the representation of isentropic mixing in ocean circulation models. *Journal of Physical Oceanography*, *1*(3), 233–234. https://doi.org/10.1175/1520-0485(1971)001<0233:OTROIM>2.0.CO;2

Sunda, W. (2012). Feedback interactions between trace metal nutrients and phytoplankton in the ocean. *Frontiers in Microbiology*, *3*(204), 6–27. https://doi.org/10.3389/fmicb.2012.00204

Tagliabue, A., Aumont, O., & Bopp, L. (2014). The impact of different external sources of iron on the global carbon cycle. *Geophysical Research Letters*, *41*, 920–926. https://doi.org/10.1002/2013GL059059

Tagliabue, A., Aumont, O., DeAth, R., Dunne, J. P., Dutkiewicz, S., Galbraith, E., et al. (2016). How well do global ocean biogeochemistry models simulate dissolved iron distributions? *Global Biogeochemical Cycles*, *30*, 149–174. https://doi.org/10.1002/2015GB005289

Tagliabue, A., Bopp, L., Dutay, J. C., Bowie, A. R., Chever, F., Jean-Baptiste, P., et al. (2010). Hydrothermal contribution to the oceanic dissolved iron inventory. *Nature Geoscience*, *3*(4), 252–256. https://doi.org/10.1038/ngeo818

Tagliabue, A., Bowie, A. R., Boyd, P. W., Buck, K. N., Johnson, K. S., & Saito, M. A. (2017). The integral role of iron in ocean biogeochemistry. *Nature*, *543*(7643), 51–59. https://doi.org/10.1038/nature21058

Tagliabue, A., & Resing, J. (2016). Impact of hydrothermalism on the ocean iron cycle. *Philosophical Transactions of the Royal Society A: Mathematical Physical and Engineering Sciences*, *374*(2081), 20150291. https://doi.org/10.1098/rsta.2015.0291

Tagliabue, A., Sallee, J. B., Bowie, A. R., Levy, M., Swart, S., & Boyd, P. W. (2014). Surface-water iron supplies in the southern ocean sustained by deep winter mixing. *Nature Geoscience*, *7*(4), 314–320. https://doi.org/10.1038/ngeo2101

Tagliabue, A., & Völker, C. (2011). Towards accounting for dissolved iron speciation in global ocean models. *Biogeosciences*, *8*(10), 3025–3039. https://doi.org/10.5194/bg-8-3025-2011

van den Berg, C. M. G. (1995). Evidence for organic complexation of iron in seawater. *Marine Chemistry*, *50*(1), 139–157. https://doi.org/10.1016/0304-4203(95)00032-M

Velasquez, I. B., Ibisanmi, E., Maas, E. W., Boyd, P. W., Nodder, S., & Sander, S. G. (2016). Ferrioxamine siderophores detected amongst iron binding ligands produced during the remineralization of marine particles. *Frontiers in Marine Science*, *3*(172), 76–90. https://doi.org/10.3389/fmars.2016.00172

Voelker, A. H. L., Colman, A., Olack, G., Waniek, J. J., & Hodell, D. (2015). Oxygen and hydrogen isotope signatures of Northeast Atlantic water masses. *Deep Sea Research Part II: Topical Studies in Oceanography*, *116*, 89–106. https://doi.org/10.1016/j.dsr2.2014.11.006

Völker, C., & Tagliabue, A. (2015). Modeling organic iron-binding ligands in a three-dimensional biogeochemical ocean model. *Marine Chemistry*, *173*, 67–77. https://doi.org/10.1016/j.marchem.2014.11.008

Vraspir, J. M., & Butler, A. (2009). Chemistry of marine ligands and siderophores. *Annual Review of Marine Science*, *1*(1), 43–63. https://doi.org/10.1146/annurev.marine.010908.163712

Wu, J., & Boyle, E. (2002). Iron in the Sargasso Sea: Implications for the processes controlling dissolved Fe distribution in the ocean. *Global Biogeochemical Cycles*, *16*(4), 1086. https://doi.org/10.1029/2001GB001453

Wu, J., Boyle, E., Sunda, W., & Wen, L.-S. (2001). Soluble and colloidal iron in the oligotrophic North Atlantic and North Pacific. *Science*, *293*(5531), 847–849. https://doi.org/10.1126/science.1059251

Wunsch, C., & Heimbach, P. (2007). Practical global oceanic state estimation. *Physica D*, *230*, 197–208.

Ye, Y., & Völker, C. (2017). On the role of dust-deposited lithogenic particles for iron cycling in the tropical and subtropical atlantic. *Global Biogeochemical Cycles*, *31*, 1543–1558. https://doi.org/10.1002/2017GB005663